Journal of Science and Technology − Smart Systems and Devices
Volume 36, Issue 3, September 2026, 067–073

Effect of Length-to-Diameter Ratio on the Hydrodynamic Resistance of an Autonomous Underwater Vehicle at Constant Displacement: A Validated Computational Fluid Dynamics Study

Danh Bui Thanh[1,2,*], He Ngo Van[1], Yoshiho Ikeda[3]
[1] Hanoi University of Science and Technology, Ha Noi, Vietnam
[2] Vietnam Maritime University, Hai Phong, Vietnam
[3]Osaka Metropolitan University, Osaka, Japan
[*]Corresponding author email: danhbt.dt@vimaru.edu.vn

Abstract

This paper examines the influence of the hull length-to-diameter ratio (L/D) on the hydrodynamic resistance of a generic axisymmetric AUV, represented by the DARPA SUBOFF bare hull. Three-dimensional steady Reynolds–averaged Navier–Stokes (RANS) simulations were conducted in STAR-CCM+ using the shear-stress transport (SST) k–ω turbulence model. The numerical procedure was validated against the SUBOFF towing-tank data of Liu and Huang: after a grid-independence study, the predicted resistance differs from the measurements by up to 3.1% across six forward speeds (1.27% at the reference condition). A family of five hulls spanning L/D = 6.44–11.76 was then generated by affine scaling at constant displacement, and each hull was simulated at six forward speeds. At every speed the resistance, expressed through a volumetric drag coefficient, has a minimum at L/D = 8.57, with off-optimum penalties below about 2%; the coefficient decreases with increasing Reynolds number. A slight change in the relative ranking of the off-optimum hulls was observed between low and high speeds, suggesting a shift in the balance between frictional and pressure-related resistance mechanisms. The findings provide quantitative guidance for selecting the slenderness of axisymmetric AUV hulls

Keywords: AUV, hydrodynamic resistance, length-to-diameter ratio, RANS.

1. Introduction

Autonomous underwater vehicles (AUVs) are now routine tools for oceanographic survey, subsea inspection, marine archaeology and defense applications. Because their endurance and range are limited by the energy carried on board, the hydrodynamic resistance that the propulsion system must overcome is a first-order constraint on performance: reducing hull drag directly increases operational range and lowers the required propulsive power [1, 2]. The external hull form, and in particular its slenderness, is therefore one of the most influential design parameters for an AUV.

Computational fluid dynamics (CFD), and especially the Reynolds-averaged Navier-Stokes (RANS) approach, has become a standard tool for AUV hull hydrodynamics because it captures viscous effects at far lower computational cost than large-eddy simulation while providing detailed flow fields that empirical methods cannot [3]. Numerous numerical and experimental studies have characterized the hydrodynamic forces on axisymmetric AUV hulls [4, 5]. The DARPA SUBOFF model is the most widely used benchmark for validating such simulations, owing to the comprehensive towing-tank database reported by Liu and Huang [6]. SUBOFF in particular has been used extensively to define the benchmark geometry and to assess appendage effects on axisymmetric bodies [7, 8].

Among the geometric parameters of an axisymmetric hull, the length-to-diameter ratio (L/D) strongly governs the balance between skin-friction drag and pressure drag [9]. Moonesun *et al.* reported an optimum *L/D* of 7-10 for submarines with a cylindrical middle body [10], and Divsalar examined modifications of the SUBOFF nose, tail and main body [11]. More recent studies have continued to pursue AUV hull drag reduction and shape optimization by CFD, and have indicated that a hull optimized at one operating condition need not remain optimal at another [1, 2, 12].

However, a systematic study that varies L/D at strictly constant displacement so that the comparison reflects hull shape rather than overall size and that is validated across a range of Reynolds numbers, remains limited. The present work addresses this gap. A constant-displacement family of SUBOFF-type hulls is generated by affine scaling, and the resistance of each hull is evaluated with a validated STAR-CCM+ RANS model at six forward speeds. A volumetric drag coefficient is adopted to ensure a fair comparison of hulls of equal displacement.

p-ISSN 3093-3285
e-ISSN 3093-3315
https://doi.org/10.51316/jst.192.ssad.2026.36.3.8
Received: Jul 22, 2026; Revised: Aug 13, 2026;
Accepted: Aug 21, 2026; Online: Aug 25, 2026

2. Baseline Geometry and Hull Variants

2.1. Baseline SUBOFF Hull

The baseline geometry is the DARPA SUBOFF bare hull (DTRC model 5470), reconstructed from the analytic definition of Groves *et al.* [7]. The overall length is L = 4.356 m and the maximum diameter is D = 0.508 m, as illustrated in Fig. 1. The hull comprises a 1.016 m forebody, a 2.229 m parallel middle body and a 1.111 m afterbody. The wetted surface area is 5.988 m^2 and the enclosed displacement is V = 0.699 m^3.

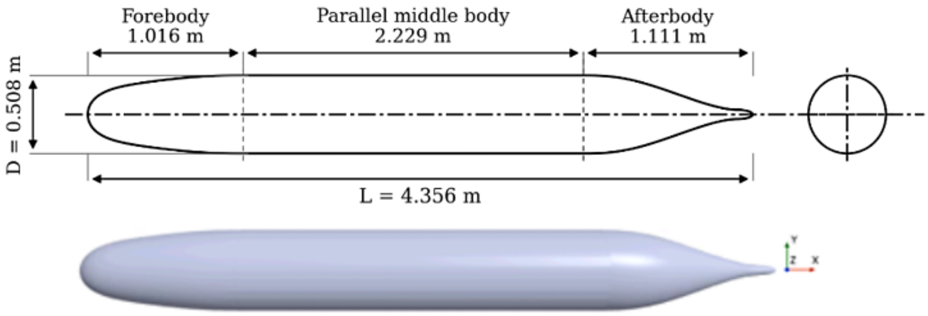

Fig. 1. The DARPA SUBOFF bare-hull model

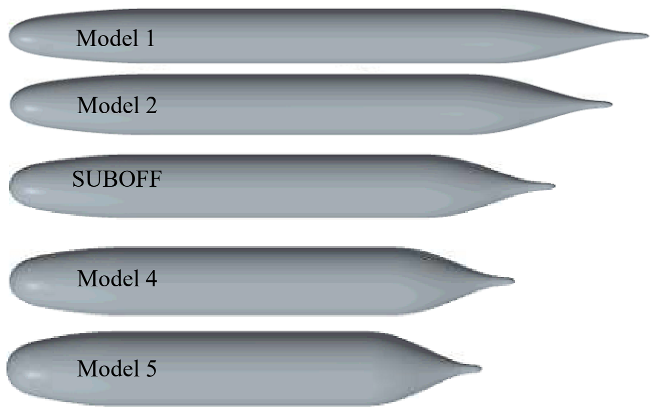

Fig. 2. The five constant-displacement hull variants

Table 1. Constant-displacement hull variants generated by affine scaling

Case	*k*	*D* (m)	*L* (m)	*L/D*
Model 1	0.90	0.4572	5.378	11.76
Model 2	0.95	0.4826	4.826	10.00
SUBOFF	1.00	0.5080	4.356	8.57
Model 4	1.05	0.5334	3.951	7.41
Model 5	1.10	0.5588	3.600	6.44

2.2. Constant-Displacement Variants

To examine the influence of slenderness while keeping the displaced volume fixed, the hull is rescaled by an affine transformation. The two transverse axes (y, z) are scaled by a factor k, which sets the new diameter, and the longitudinal axis (x) is scaled by $1/k^2$. Because the volume of an affinely transformed body changes by the product of the three scale factors, the displacement is preserved exactly for any value of k.

$$\frac{V_{new}}{V} = s_x \cdot s_y \cdot s_z = \frac{1}{k^2} \cdot k \cdot k = 1 \qquad (1)$$

where s_x, s_y and s_z are the scale factors applied along the longitudinal (x) and the two transverse (y, z) axes, respectively, with $s_x = 1/k^2$ and $s_y = s_z = k$. Scaling y and z by the same factor keeps every cross-section circular, so each variant remains a body of revolution. Five values, k = 0.90-1.10, yield the hulls listed in Table 1, whose length-to-diameter ratios range from 6.44 to 11.76. The entire hull (fore, parallel and aft bodies) is stretched affinely by the same factors, so the length ratios of the three sections are preserved and no section is modified individually; consequently, the forebody and afterbody become correspondingly finer or blunter as the diameter changes. The new five models are illustrated in Fig. 2.

3. Numerical Method

3.1. Numerical Setup

The flow is treated as steady, incompressible and turbulent, and is governed by the RANS equations. Turbulence closure is provided by Menter's shear-stress transport (SST) k-omega model [13], which blends the k-omega formulation near the wall with the k-epsilon formulation in the free stream. This combination is well suited to the adverse pressure gradients and incipient separation that occur on streamlined bodies of revolution. The all-y^+ wall treatment is used so that the near-wall region is resolved consistently across the mesh.

The working fluid is water at 18°C, with density ρ = 998.55 kg/m^3 and dynamic viscosity μ = 1.053x10^{-3} Pa·s. A steady, segregated solver is used with the SIMPLE algorithm for pressure-velocity coupling and second-order upwind discretization of the convective terms.

The computational domain is a rectangular prism sized relative to the hull length (*L*), extending *3L* upstream, *5L* downstream, and *3L* laterally to ensure undisturbed development of the flow field without compromising numerical accuracy. Boundary conditions include a velocity inlet set to experimental speeds ranging from 5.92 to 17.99 knots and a pressure outlet at zero-gauge pressure. The hull is modelled as a no-slip wall to capture boundary layer physics, while symmetry planes are utilized at the outer boundaries to optimize computational efficiency. The computational domain is shown as in Fig. 3.

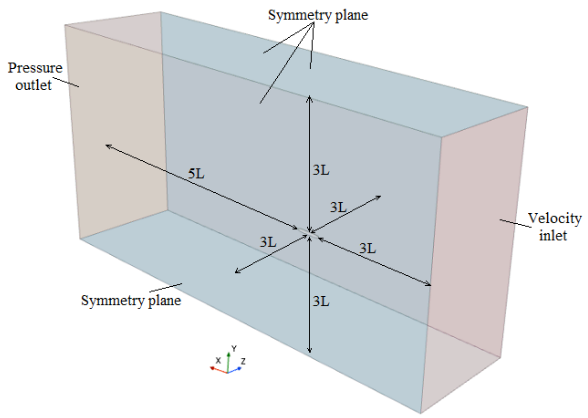

Fig. 3. The computational domain

The computational domain was discretized using trimmed hexahedral cells with prism layers near the hull surface. This near-wall refinement is critical for accurately capturing the viscous effects and pressure gradients within the boundary layer. The prism layers are applied around the model with 1.3 stretching, and the total thickness is 0.1 m with a base size of 1.0 m. The first-layer thickness yields an average wall y^+ of about 4, within the range handled by the all-y^+ wall treatment. For the variant hulls, the refinement zones were enlarged to enclose the largest body, and identical mesh settings were applied to every case so that differences in resistance reflect the hull shape rather than the mesh. The mesh generation of the DARPA SUBOFF bare-hull model is given in Fig. 4.

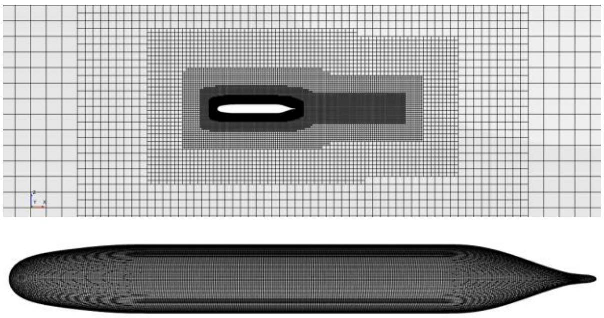

Fig. 4. The mesh generation

3.2. Grid-Independence Study

The baseline hull was tested at v = 6.091 m/s (Re = 2.52×10^7) on a sequence of successively refined meshes. As the base size is reduced, the predicted resistance falls steadily and then levels off once the near-wall region is fully resolved ($y^+ \approx 4$); beyond 1.44 million cells the value is essentially fixed, changing by under 0.05% up to the finest grid tested. The 1.44-million-cell mesh was therefore adopted for all production runs, giving a resistance of 328.7 N (1.27% above the measured value) at a moderate computational cost. Representative meshes are listed in Table 2.

The numerical uncertainty associated with grid discretization was assessed following the ITTC verification framework [14], using four wall-resolved meshes of 1.44, 1.71, 2.13 and 2.68 million cells ($y^+ \approx 4$) with an unchanged prism-layer distribution. The predicted resistance varies non-monotonically within a bounded range of 0.05 N (328.62–328.67 N), the successive differences changing sign without growing under refinement. Richardson extrapolation, and hence the Grid Convergence Index derived from it, presumes monotonic convergence and is therefore not applicable to this sequence. Following the ITTC treatment of oscillatory convergence, the uncertainty is estimated from half the oscillation amplitude, $U_G \approx 0.03$ N (0.01% of the baseline resistance), two orders of magnitude below the resistance differences of up to about 2% between the hull variants (Table 3). Identical meshing parameters were used for all five hulls (Section 3.1), so this error is largely systematic and cancels in the hull-to-hull comparison; the same minimum recurs at all six speeds (Section 4.1).

Table 2. Grid-independence study for the baseline hull at v = 6.091 m/s

Mesh	**Cells ($\times10^6$)**	**y+**	**Resistance (N)**	**Deviation (%)**
Coarse	0.30	190	358.0	7.55
Intermediate	0.82	37	340.9	2.42
Fine	1.44	3.84	328.67	1.27
Fine 2	1.71	3.85	328.63	1.28
Finer	2.13	3.85	328.62	1.29
Finest	2.68	3.85	328.67	1.27

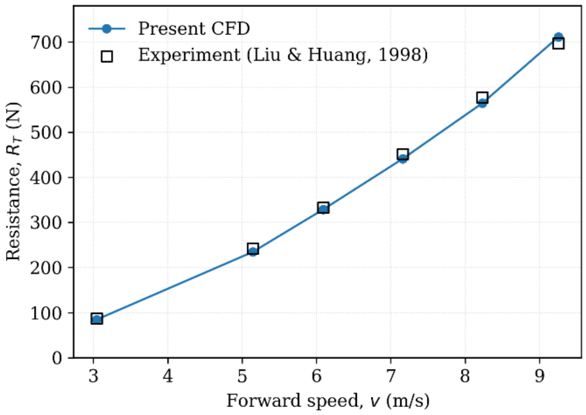

Fig. 5. Comparison of the computed and measured resistance of the baseline SUBOFF hull over six forward speeds (Re = 1.26–3.82×10⁷), Experimental data from Liu and Huang [6]

The baseline resistance computed with the Fine mesh was compared with the towing-tank measurements of Liu and Huang [6] at six forward speeds, as displayed in Fig. 5. The deviation ranges from 1.27% to 3.13%, confirming the accuracy of the numerical procedure. The numerical solving procedure and turbulence model are therefore considered to have acceptable accuracy for the present study.

4. Results and Discussion

4.1. Effect of L/D on Resistance

Table 3 lists the resistance of the five hulls over the six forward speeds. At each speed the resistance is lowest at the baseline slenderness (*L/D* = 8.57) and rises for both more slender and blunter hulls, although the variation across the family is modest, remaining below about 2%. Fig. 6 plots the resistance against *L/D*, and Fig. 7 against forward speed for each hull.

The optimum *L/D* found here, close to 8.5, lies within the range of 7-10 reported by Moonesun *et al.* for submarines with a cylindrical middle body [10]. The fact that the baseline SUBOFF hull is already near the optimum explains the relatively small variation of resistance across the family. This agreement, together with the experimental validation of Section 4, supports the reliability of the present constant-displacement methodology.

Table 3. Resistance of the five hulls at six forward speeds

	v (m/s)	**3.045**	**5.144**	**6.091**	**7.161**	**8.231**	**9.255**
	L/D			**Resistance (N)**			
Model 1	11.76	86.0	237.1	332.8	447.4	574.6	724.4
Model 2	10.00	85.0	235.0	329.5	442.6	567.3	715.1
SUBOFF	8.57	84.7	234.6	328.7	441.1	564.2	711.1
Model 4	7.41	85.0	236.3	330.6	443.4	565.8	713.2
Model 5	6.44	86.0	239.4	334.8	448.7	571.7	720.1

Table 4. Volumetric drag coefficient CD_v (x10^{-3}) of the five hulls at six forward speeds

	v (m/s)	**3.045**	**5.144**	**6.091**	**7.161**	**8.231**	**9.255**
	L/D				**CD_v**		
Model 1	11.76	23.59	22.79	22.82	22.19	21.57	21.51
Model 2	10.00	23.32	22.59	22.59	21.95	21.30	21.23
SUBOFF	8.57	23.23	22.55	22.53	21.88	21.18	21.11
Model 4	7.41	23.32	22.71	22.66	21.99	21.24	21.18
Model 5	6.44	23.59	23.01	22.95	22.25	21.46	21.38

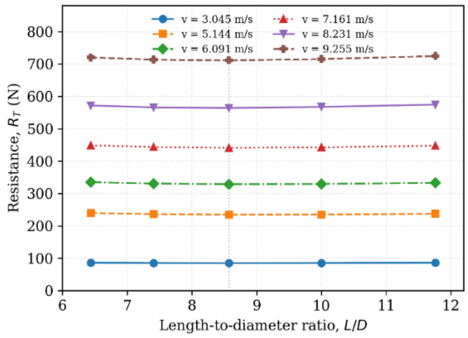

Fig. 6. Resistance versus length-to-diameter ratio at each forward speed

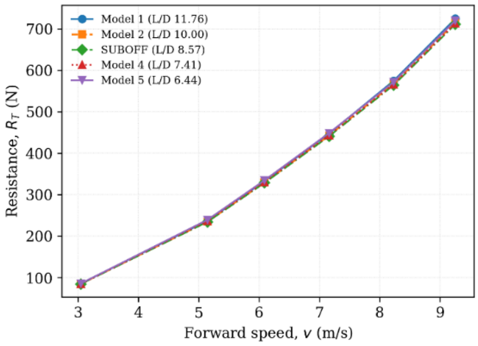

Fig. 7. Resistance versus forward speed for the five hull variants

4.2. Volumetric Drag Coefficient

Because the five hulls have the same displacement, the volumetric drag coefficient CD_v is the appropriate metric for comparing hull efficiency. As shown in Fig. 8 and Table 4, CD_v has a minimum at $L/D = 8.57$ at all six speeds, and decreases from about 0.0232 at $v = 3.045$ m/s to 0.0211 at $v = 9.255$ m/s, reflecting the usual reduction of the skin-friction coefficient with increasing Reynolds number. It should be noted that a drag coefficient based on wetted area would instead decrease monotonically with slenderness and could misleadingly suggest that the most slender hull is best; since slender hulls have a larger wetted area, however, their total resistance is in fact higher. The volumetric coefficient, by removing only the common displacement, preserves the physically meaningful ranking obtained from the resistance itself.

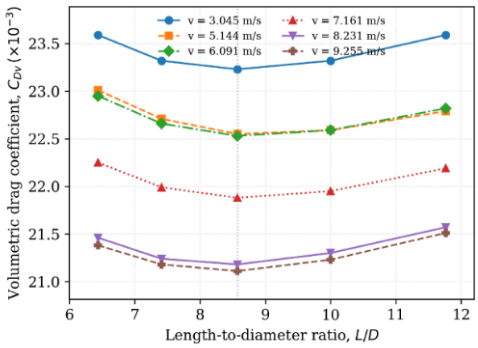

Fig. 8. Volumetric drag coefficient versus length-to-diameter ratio

Table 5. Friction fraction R_f/R_T (%) of the five hulls at three forward speeds

	L/D	**v = 3.045 m/2**	***v* = 6.091 m/s**	***v* = 9.255 m/s**
		Rf/RT (%)		
Model 1	11.76	91.1	90.9	92.2
Model 2	10.00	89.0	88.9	90.3
SUBOFF	8.57	86.7	86.6	88.1
Model 4	7.41	84.0	83.9	85.7
Model 5	6.44	81.0	81.0	82.9

The existence of an optimum reflects the well-known trade-off between skin-friction and form drag. A more slender hull has a larger wetted surface area and therefore higher skin-friction drag, whereas a blunter hull develops a stronger adverse pressure gradient towards the stern, increasing the form (pressure) drag and the risk of flow separation. The minimum resistance occurs where these two contributions are balanced.

The friction fraction R_f/R_T is nearly independent of speed, at each *L/D* it varies by only one to two percentage points across the range, as shown in Table 5, increasing marginally at the highest speed. This confirms that the friction-dominated balance and hence the optimum at $L/D = 8.57$ is preserved over the full Reynolds-number range. The only residual effect is a small, second-order change in the ranking of the off-optimum hulls: the blunter hull (low *L/D*) incurs the larger penalty at the lower speeds, whereas the more slender hull (high *L/D*) becomes the more penalized at the highest speeds, the change of ranking occurring near v = 7-8 m/s. The differences between the off-optimum hulls are small, below about 2%, and approach the numerical uncertainty of the simulations, so this trend is reported as a qualitative observation; it is nonetheless consistent with reports that a hull optimized at one operating condition need not remain optimal at another [1, 2].

4.3. Flow-field Interpretation Based on Dynamic-Pressure Contours

Table 6 separates the total resistance (RT) into its pressure (Rp) and friction (Rf) components at v = 6.091 m/s. Skin friction dominates for all hulls, contributing 81–91% of the total. As *L/D* increases from 6.44 to 11.76, the friction resistance rises from 271.1 to 302.6 N with the larger wetted area, while the pressure resistance falls from 63.7 to 30.2 N as the afterbody pressure gradient weakens. Because these two contributions vary in opposite directions, the total resistance is minimized at an intermediate value, L/D = 8.57 (328.7 N). The decomposition thus identifies the skin-friction/form-drag balance as the origin of the optimum.

Table 6. Decomposition of the total resistance into pressure and friction components at v = 6.091 m/s

Model	***L/D***	**R_p (N)**	**R_f (N)**	**R_T (N)**	**R_f/R_T (%)**
Model 1	11.76	30.2	302.6	332.8	90.9
Model 2	10.00	36.7	292.8	329.5	88.9
SUBOFF	8.57	44.2	284.5	328.7	86.6
Model 4	7.41	53.2	277.4	330.6	83.9
Model 5	6.44	63.7	271.1	334.8	81.0

The dynamic pressure distributions of the five hull variants at v = 6.091 m/s are shown in Fig. 9. Since the flow is incompressible, high dynamic pressure corresponds to low static pressure, so the field also indicates where the adverse pressure gradient towards the stern is strongest. The overall flow topology is similar for all configurations, dynamic pressure vanishes at the nose stagnation point, rises to a maximum over the forebody shoulder where the flow accelerates, and falls again in the low-momentum near wake, but the bow, stern and wake regions differ in detail with hull slenderness.

For the slender hulls (Models 1 and 2, *L/D* = 11.76 and 10.00), the dynamic-pressure variation is distributed over a greater length and the deceleration towards the stern is more gradual, producing a weaker adverse pressure gradient. However, the greater length increases the wetted surface area and the extent of boundary-layer development, which amplifies the viscous contribution to resistance.

For the blunterhulls (Models 4and 5, *L/D* = 7.41 and 6.44), the cross-sectional area changes more rapidly along the hull. This produces stronger flow acceleration and deceleration near the stern and a broader low-dynamic-pressure region in the near wake. These features are consistent with the larger pressure-drag contribution reported quantitatively in Table 6.

The baseline SUBOFF hull (*L/D* = 8.57) exhibits an intermediate dynamic-pressure field: the deceleration towards the sternis moregradual than fortheblunthulls, while the hull is not as long as the slender variants. This is consistent with the resistance results of Section 4.1, in which the baseline hull has the lowest resistance of the five configurations.

In summary, the contours support the view that the numerically determined optimum near *L/D* = 8.57 arises from a balance between two competing mechanisms: increasing slenderness relieves the adverse pressure gradient but increases viscous drag, whereas decreasing slenderness shortens the hull but steepens the adverse pressure gradient and strengthens the wake.

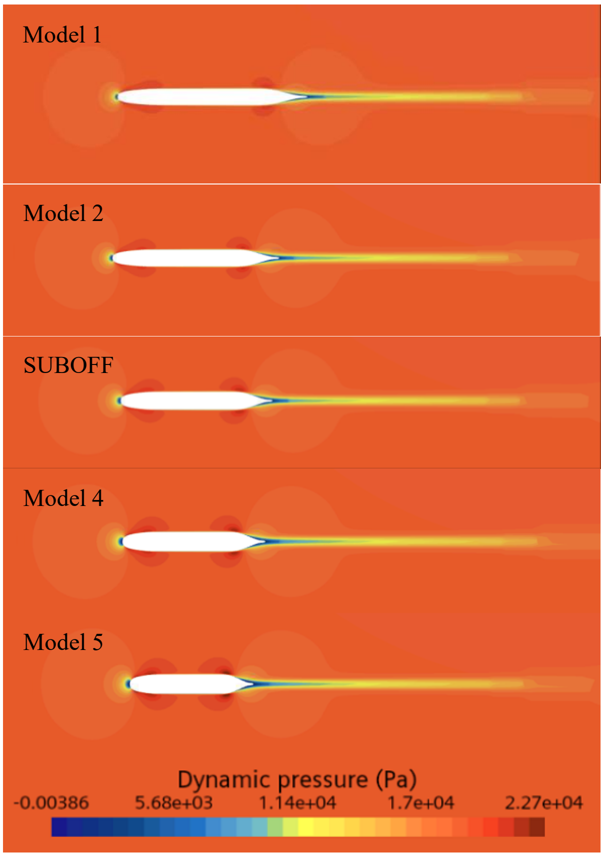

Fig. 9. Dynamic pressure distribution for five different models at v = 6.091 m/s

5. Conclusion

A validated CFD study of the effect of the length-to-diameter ratio on the resistance of an axisymmetric, SUBOFF-type AUV hull has been presented. The main findings are as follows:

(i) The STAR-CCM+ RANS procedure with the SST k-omega model reproduces the SUBOFF towing-tank resistance to within 3.1% over six speeds and is grid-independent at 1.44 million cells.

(ii) An affine-scaling transformation generates a family of hulls of exactly equal displacement, isolating the effect of slenderness from that of size.

(iii) The resistance, and equivalently the volumetric drag coefficient, exhibits a minimum at *L/D* = 8.57 at all speeds, with off-optimum penalties below about 2%; the volumetric drag coefficient decreases with increasing Reynolds number, and the more penalized hull shifts from the blunter form at low speed to the slender form at high speed.

(iv) The optimum range is consistent with the value of 7-10 reported in the literature, and the baseline SUBOFF hull is shown to be near-optimal. These results provide quantitative guidance for selecting the slenderness of axisymmetric AUV hulls.

Future work will extend the analysis to the nose and tail shapes and to nose-mounted flow-control devices such as a wedge.

Acknowledgments

This research is funded by Hanoi University of Science and Technology (HUST) under project number T2025-PC-038. The authors would like to warmly thank you for your support.

References

[1] X. Li, D. Zhang, M. Zhao, X. Wang, and Y. Shen, Hydrodynamic analysis and drag-reduction design of an unmanned underwater vehicle based on computational fluid dynamics. Journal of Marine Science and Engineering, 2024. vol. 12, iss. 8, Aug. 2024. https://doi.org/10.3390/jmse12081388

[2] G. Fan, X. Liu, Y. Hao, G. Yin, and L. He, Optimized hydrodynamic design for autonomous underwater vehicles. Machines, vol 13, iss. 3, Feb. 2025. https://doi.org/10.3390/machines13030194

[3] L. Hong, X. Wang, and D.-S. Zhang, CFD-based hydrodynamic performance investigation of autonomous underwater vehicles: A survey. Ocean Engineering, vol. 305, Aug. 2024. https://doi.org/10.1016/j.oceaneng.2024.117911

[4] P. Jagadeesh, K. Murali, and V. G. Idichandy, Experimental investigation of hydrodynamic force coefficients over AUV hull form. Ocean Engineering, vol. 36, iss. 1, pp. 113–118, Jan. 2009. https://doi.org/10.1016/j.oceaneng.2008.11.008

[5] T. Gao, Y. Wang, Y. Pang, Q. Chen, and Y. Tang, A time-efficient CFD approach for hydrodynamic coefficient determination and model simplification of submarine. Ocean Engineering, vol. 154: pp. 16–26, Apr. 2018. https://doi.org/10.1016/j.oceaneng.2018.02.003

[6] H. Liu, T. T. Huang, Summary of DARPA SUBOFF Experimental Program Data. Technical Report. Jun. 1998.

[7] N. C. Groves, T. T. Huang, and M. S. Chang, Geometric characteristics of DARPA SUBOFF Models (DTRC Model NOS. 5470 and 5471). Mar. 1989.

[8] Wang, Y., T. Gao, Y. Pang, and Y. Tang, Investigation and optimization of appendage influence on the hydrodynamic performance of AUVs. Journal of Marine Science and Technology, vol. 24, iss. 1, pp. 297–305, Mar. 2019. https://doi.org/10.1007/s00773-018-0558-y

[9] P. Stevenson, M. Furlong, and D. Dormer, AUV shapes - combining the practical and hydrodynamic considerations. Oceans 2007 - Europe. IEEE, Sep. 2007. https://doi.org/10.1109/OCEANSE.2007.4302483

[10] M. Moonesun, A. Mahdian, Y. M. Korol, M. Dadkhah, M. Javadi,and A. Brazhko, Optimum L/D for submarine shape. Indian Journal of Geo-Marine Sciences, vol. 45, iss. 1, pp. 38–43, Jan. 2016.

[11] K. Divsalar, Improving the hydrodynamic performance of the SUBOFF bare hull model: a CFD approach. Acta Mechanica Sinica, vol. 36, iss. 1, pp. 44–56, Feb. 2020. https://doi.org/10.1007/s10409-019-00913-7

[12] D. Zhang, X. Wang, M. Zhao, L. Hong, and X. Li, Numerical investigation on hydrodynamic characteristics and drag influence of an open-frame remotely operated underwater vehicle. Journal of Marine Science and Engineering, vol. 11, iss. 11, Nov. 2023. https://doi.org/10.3390/jmse11112143

[13] Menter, F.R., Two-equation eddy-viscosity turbulence models for engineering applications. AIAA Journal, vol. 32, no. 8, pp. 1598–1605, Aug. 1994. https://doi.org/10.2514/3.12149?

[14] ITTC Recommended Procedure 7.5-03-01-01, Uncertainty Analysis in CFD Verification and Validation Methodology and Procedures, 2021. [Online]. Available: https://www.ittc.info/media/9765/75-03-01-01.pdf